Khairy, M, Mahmoud, KG, Rashwan, FA, El-Sagher, HM and Banks, CE OR-CID logoORCID: https://orcid.org/0000-0002-0756-9764 (2022) Nanosized nickel hexacyanoferrate modified screen-printed electrodes as flexible su-percabattery platforms: Influence of annealing temperatures and supporting electrolytes. Journal of Energy Storage, 46. p. 103872. ISSN 2352-152X

Nanosized nickel hexacyanoferrate modified screen-printed electrodes as flexible supercabattery platforms: Influence of annealing temperatures and supporting electrolytes

Mohamed Khairy [a], Khaled G. Mahmoud [a], Farouk A. Rashwan [a], Hussein M. El-Sagher [a], Craig E. Banks [b]

[a] Chemistry Department, Faculty of Science, Sohag University 82524, Egypt

[b] Faculty of Science and Engineering, Manchester Metropolitan University, Chester, Manchester, Northern Ireland M1 5GD, United Kingdom

Corresponding author:

mohamed.khairy@science.sohag.edu.eg

Abstract

Water-insoluble nickel hexacyanoferrate $Ni_3[Fe(CN)_6]_2 \cdot nH_2O$ (NiHCF) nanoparticles were synthesized via a facile precipitation method in the presence of polyvinylpyrrolidone (PVP) and sodium citrate (SC). Large-scale production of cubic NiHCF crystals with an average diameter of 35 nm and a specific surface area (S_{BET}) of 452.9 m2/g was shown to be possible. The NiHCF nanoparticles were drop-cast upon screen-printed graphite macroelectrode surfaces (SPEs) allowing a flexible energy storage device to be realised. The tunable pore size and dual functional reactive sites offered superior specific capacitances of 197.5, 139.35, 356.25, and 406.25 F/g in 0.1 M KCl, 0.1 M NaCl, 0.1 M NaOH and 0.1 M KOH, respectively at a current density of 5 A/g. The highest capacitance was found using 0.1 M KOH supporting electrolyte due to the combination of surface (intercalation/de-intercalation of A^+) and faradaic processes (M^{2+}/M^{3+}) as supercabattery platforms. The thermal treatment of the NiHCF samples at 100, 200, 300 °C were performed within oxygen and nitrogen atmospheres and the specific capacitances were measured in 0.1 M KOH. Interestingly, the specific capacitance increases up to 546 F/g for NiHCF annealed at 100 °C in oxygen and reduces to 342 F/g if NiHCF when annealed at 200 °C in nitrogen atmospheres due to the likely introduction of diverse vacancies. Furthermore, the NiHCF/SPEs were investigated in an as-symmetric two-electrode system, which revealed a specific capacitance of 570 F/g at 5 A/g. The NiHCF/SPE exhibited high capability rate, capacitive retention and excellent cycling stabilities particularly if NiHCF was annealed within a nitrogen atmosphere. Thus, the NiHCF supercabattery platforms can be used for developing new flexible energy storage devices.

Introduction

Energy storage systems are urgently required to satisfy the global growth of energy demands to power electric vehicles/devices as well as storing renewable electrical energy that is produced from different sources such as wind, solar or thermal energies [1]. Amongst the energy storage devices, supercapacitors can deliver higher power density, reliable charge-discharge efficiency and excellent cycling stability (> 10,000) in comparison with rechargeable batteries [2,3]. These features are originated from the unique charge storage mechanism via surface reaction of the electrode materials without mass transfer of ions within the bulk of the electrodes. Thus, supercapacitor devices could be considered as a complement energy-storage system to rechargeable batteries and fuel cells [4]. Different nanostructured materials such as transition metal oxides (e.g. RuO2, Fe2O3, MnO2, CdO, NiO, V2O5) [[5], [6], [7]], transition metal chalcogenides (MoS2, MoSe2, WS2), MXenes (Ti3C2Tx) and conductive polymers (e.g. polyaniline, polythiophene, polypyrrole) have been used as the basis of supercapacitors [[8], [9], [10], [11]].

Prussian blue and its analogues (PBAs) are a class of metal-organic frameworks with a perovskite-like structure, can be described by a general chemical formula $AxMy[Fe(CN)_6]z. nH2O$, $0 \leq x$ and $y \geq 2$; $y < 1$, where A is an alkali metal and M is a transition metal. PBAs exhibit open framework structures with well-dispersed interstitial active sites and charge states since nitrogen-coordinated with metal ions (M) and carbon-coordinated iron sites bridged with cyanide linker. Such unique intrinsic three-dimensional opening structure, nontoxicity, easy preparation and low cost of the components offered diverse potential applications such as pigments [12], drug delivery [13], cancer theragnostics [14], removal of radioactive [15], sensors [16], water splitting [17], oxygen evolution catalyst [18] and metal-ion batteries [19,20]. Amongst these applications, the development of energy storage devices based on PBAs find more interest recently because it can easily manipulate the active metals, generate vacancies, which enhanced the stability, ionic conductivity and facilitate ion insertion. Additionally, PBAs also can be used as sacrificial precursors for synthesis of metal oxides, metal sulphides, and graphitic carbon nitride that are commonly utilized in energy storage systems. The PBAs can be classified to insoluble with a formula of $Fe_3[Fe(CN)_6]_2 \cdot xH_2O$, x = 14–16 and soluble with a formula of A4-yFey[Fe(CN)6]·zH2O, y = 0–1. The water-soluble PBAs were extensively used as a cathode electrode in Na+, K+, Mg2+ and Al3+- ion batteries [21]. Transition metal ions in the outer sphere and water molecules mainly control the efficiency of alkali metal diffusion and intercalation in the open framework. Numerous synthesis methods such as precipitation, hydrothermal, sonochemical and microemulsion were utilized [2]. Further, mesoporous PBA with relatively large surface areas from 93

to 299 m2/g was prepared by controlling the reaction time [22]. Zhang et al., synthesized PBA nanoframes by controlled preferential etching of Mn+ or [Fe(CN)6]4- with 30 m2/g for sodium-ion batteries [23]. On the other hand, very few literatures reported water-insoluble PBAs for supercapacitor applications. Yin et al., synthesized hollow-cobalt hexacyanoferrate with a surface area of 166 m2/g for Na-ion supercapacitor in Na2SO4 and showed a specific capacitance of 284 F/g at 1.0 A/g [24]. Chen et al. prepared Ni3[Fe(CN)6]2 H2O nanoparticles by slowly mixing of K3[Fe(CN)6] and Ni(NO3)2•6H2O and revealed a specific capacitance of 574.7 F/g at 0.2 A/g in 1.0 M KNO3 at a narrow potential range from 0.3 to 0.6 V [25]. However, the stability is reduced with charge/discharge cycling and the potential range of the capacitance measurement is very low.

Herein, a water-insoluble nickel hexacyanoferrate (Ni3[Fe(CN)6]2.H2O) nanoparticle was synthesized by a facile precipitation method in presence of polyvinylpyrrolidone (PVP) and sodium citrate (SC) and then used to modify flexible screen-printed graphite macroelectrodes (SPEs) for the first time. The PVP and SC are utilized to limit the nucleation rate and minimize the concentration of [Fe(CN)6] vacancies and coordinated water in the PBA framework which might lead to improved coulombic efficiency and specific capacity for energy storage devices based on PBA [26]. Different $Ni2+$: $[Fe(CN)_6]^{3-}$ ratios were prepared and explored for energy-storage applications in different supporting electrolytes of KCl, NaCl, NaOH, and KOH. A promising specific capacitance is observed in a ratio of $Ni2+$: $[Fe(CN)_6]^{3-}$ to be (1.5:1) in 0.1 M KOH. Furthermore, the NiHCF sample (S2) with a high capacitance was annealed at 100, 200, 300 °C in oxygen and nitrogen atmospheres. The annealed NiHCF samples were explored as the basis of energy storage systems.

Experimental section

Chemicals

All chemicals were of the highest analytical grade and used without further purification. Nickel (ll) nitrate hexahydrate ($Ni(NO_3)_2 \cdot 6H2O$), polyvinylpyrrolidone (PVP), trisodium citrate dihydrate (SC), potassium hexacyanoferrate(III) (PHCF, $K_3[Fe(CN)_6]$), polytetrafluoroethylene (PTFE), carbon black, potassium hydroxide (KOH), sodium hydroxide (NaOH), potassium chloride (KCl), sodium chloride (NaCl) and ethanol absolute were purchased from sigma Aldrich CO LTD. All solutions were prepared by double distilled water with a specific resistance > 18 MΩ cm.

Synthesis of nickel hexacyanoferrate (NiHCF) and its analogues

Different molar ratios of Ni2+: SC: PHCF were prepared as follows; sample (S1; 1:1:1), sample (S2; 1.5:1.5:1) and sample (S3; 2:2:1), respectively. For example, S2 was synthesized by dissolving 300 mg PVP, 150 mg SC, and 175 mg Ni(NO3)2•6H2O in 20 mL doubly distilled water. The mixture was stirred for 10 min. A 132 mg of PHCF was dissolved in 20 mL water. The PHCF solution was added dropwise to the mixture under magnetic stirring for one hour. The mixture was left for 24 h at room temperature and a centrifuge at 10,000 rpm for 20 min separated the resulting precipitate. The precipitate was washed several times by water/ethanol mixture and dried at 50 °C to remove residual SC and PVP. For thermal treatment, S2 was annealed at 100 °C, 200 °C, and 300 °C for 2.0 h in air and nitrogen atmosphere in muffle and tube furnace, respectively with a heating rate of 2 °C/min. The PBA samples left to cool to room temperature for further experiments. Further, the NiHCF sample (S2) was also synthesised with different citric ratio of 250 mg (S4) and 350 mg (S5) to obtain different particle size as suggested previously [27].

Preparation of flexible screen-printed graphite macroelectrodes modified by PBAs

The flexible graphite screen-printed electrodes (3.1 mm diameter) were fabricated using appropriate stencil using a DEK 248 screen-printing machine (S1 in supporting information) [28,29]. Three-electrode configuration (carbon counter and Ag/AgCl reference) was prepared with carbon ink working, counter electrodes and silver/silver chloride reference electrodes. A suspension solution was prepared by mixing 80% of NiHCF or its analogues with 10% carbon black and 10% PTFE. A 5 μL sample of NiHCF or its analogues suspension drop-cast on the screen-printed surface and left to dry for 30 min in electric furnace at temperature 50 °C.

Characterization of NiHCF and its analogues

The morphology of NiHCF and its analogues were characterized using Field emission scanning electron microscopy (ZEISS model Sigma 500). The samples were grinded and fixed onto a specimen of double-sided carbon tape. A 10 nm Pt film was deposited via anion sputtering at room temperature to obtain high-resolution images. The SEM operated at 30 kV to obtain high-resolution images. The energy dispersed X-ray spectroscopy (EDX) of NiHCF samples was carried out at a scanning electron microscopy (SEM) model JEOL 5400 LV operated at 15 kV. Further, transmission electron microscopy (TEM) images were carried out at a JEOL JEM model 2100F microscope. The TEM operated at an acceleration voltage of 200 kV to obtain a lattice resolution of 0.1 nm and a spherical aberration of 1.0 mm. NiHCF sample dispersed in ethanol solution using an ultrasonic cleaner, and then dropped on a copper grid. Prior to inserting the samples into the TEM column, the grid was dried for 10 min in a vacuum.

Wide-angle powder X-ray diffraction (XRD) patterns were performed using an X-ray diffractometer, model D8-Advance with monochromatic CuKα radiation (λ= 1.54 Å). The XRD patterns were measured by employing a scanning speed of 2° min^{-1} and 2θ range of 10° to 80°. The diffraction data were analysed using the DIFRAC plus Evaluation Package (EVA) software with the PDF-2 Release 2009.Fourier transform infrared spectroscopy (FTIR) was performed on Bruker ALPHA II compact FTIR spectrometer. The FTIR spectra of the NiHCF samples were recorded in the range from 400 to 4000 cm^{-1}.

The textural properties of NiHCF and its analogues were analysed by measurement of nitrogen adsorption/desorption isotherm using BELSORP mini-analyser, BEL Co., JP Ltd at 77 K. The specific surface area (SBET) was estimated by using Brunauer–Emmett–Teller (BET) method with multipoint adsorption data from the linear segment of the nitrogen adsorption isotherm. The pore-size distribution was determined by Barrett-Joyner-Halenda (BJH) method via analysis of the desorption branch. Thermal gravimetric analysis (TGA) was measured by using TG-60, Shimadzu Ltd, Japan in a flow of nitrogen and air atmospheres with scan of 10 °C/min. To illustrate the NiHCF structure, bulk analysis using inductively coupled plasma optical emission spectroscopy (ICP-OES) model Perkin Elmer Optima 8300. A particular amount of NiHCF samples were dissolved in aqua regia at 100 °C. The concentration of nickel and iron ions in NiHCF samples were measured according to a standard method of 3120B for metals in water by ICP-OES.

The electrochemical experiments were performed using IVIUM Compact Stat. potentiostat/galvanostat workstation controlled by IVIUM software. Cyclic voltammetry (CV) and galvanostatic charge/discharge techniques were carried out at room temperature. The specific capacitance (Cs) was calculated from cyclic voltammetry using the following equation:

$$C_s = \frac{1}{vm\,(\Delta V)} \int_{V_a}^{V_c} iVdV$$

The specific capacitance was calculated also by galvanostatic charge/discharge techniques as follows:

$$C_s = \frac{It}{m\,(\Delta V)}$$

The energy density (E) and power density was estimated by:

$$E = \frac{1}{2}C_s\,(\Delta V)^2$$

$$P = \frac{E}{\Delta t}$$

where Cs is specific capacitance in F/g, v is the potential scan rate in V/s, ΔV is the potential window between Va and Vc, m is the mass loading of active species, Δt is the discharge time in seconds and I is the applied discharge current in Ampere.

Results and discussion

Characterization of NiHCF samples

Control over the morphology and particle size of NiHCF is performed by using a structure-directing agent, PVP, in presence of a complexing agent of citrate ions. The citrate ion competes $[Fe(CN)_6]^{3-}$ to bonded with Ni^{2+} ions. Additionally, the PVP molecules enclose the formed crystals, coordinate with Fe^{3+} at the edges of NiHCF crystals and retard the nuclei formation. Thus, the concentration of $[Fe(CN)_6]^{3-}$ vacancies and coordinated water in the PBA framework could be reduced. Fig. 1 shows the scanning electron microscopy images of NiHCF and its analogues. Spherical nanoparticles with an average size of 35 nm were observed for NiHCF prepared by different molar ratios of Ni^{2+}: PHCF as 1:1 and 1.5:1, denominated as S1 and S2, respectively. After thermal treatment in air and nitrogen, a slight reduction of 5 nm in particle sizes is perceived without a change in spherical particle morphology. The reduction in particle size is due to the loss of hydrated water in NiHCF frameworks. Fig. 2 shows transmission electron microscopy of as-prepared NiHCF (S2) and after treated at 100 °C in air. The TEM micrographs revealed aggregated spherical particles with an average size of 35 and 30 nm for as-prepared NiHCF(S2) and after annealing in air at 100 °C. Fig. 2 (B, and D) displays different crystalline domains with discontinuous atomic arrangements distinguished in a dark colour, which might suggest the presence of vacancies or trace amount of PVP in between as a faint colour. To investigate the formation of vacancies, the bulk analysis of NiHCF components (iron and nickel ions) is determined by using inductively coupled plasma optical emission spectroscopy (ICP-OES) and combined with thermal gravimetric analysis (shown in Table S2, Figs. S2 and 3A). For NiHCF (S2), the Fe/Ni ratio is constant in bulk and surface analysis performed by ICP-OES, and EDX, respectively, indicating a prefect NiHCF crystal structure. Furthermore, it is found the atomic ratio of Fe/Ni in bulk analysis is almost stable after annealing at 100 °C in oxygen and 200 °C in nitrogen by ICP-OES. However, the atomic ratio of Fe/Ni is increased by 42.5% and 8.5% after annealing at 100 °C in oxygen and 200 °C in nitrogen as shown by EDX. Indicating the presence of Fe atoms in a high ratio compared to Ni atoms on the NiHCF crystal surface and leaves various $[Fe(CN)_6]$ vacancies inside the crystal [18]. Since no nickel atom loss during the annealing process of NiHCF, the atomic ratio of N/Ni was also calculated by EDX (Fig. S2). Significant reduction of N/Ni ratio is found after annealing at 100 °C in oxygen compared to 200 °C in nitrogen indicates losing of CN groups at the surface. This result indicates that, the nitrogen gas suppresses the [Fe(CN)6] vacancies even after annealing at 200 °C.

Fig. 1. Scanning electron microscopy images of (A) S1, (B) S2, (C) S2 of NiHCF annealed at 100 °C in air atmosphere, and (D) S2 of NiHCF annealed at 200 °C in nitrogen atmosphere.
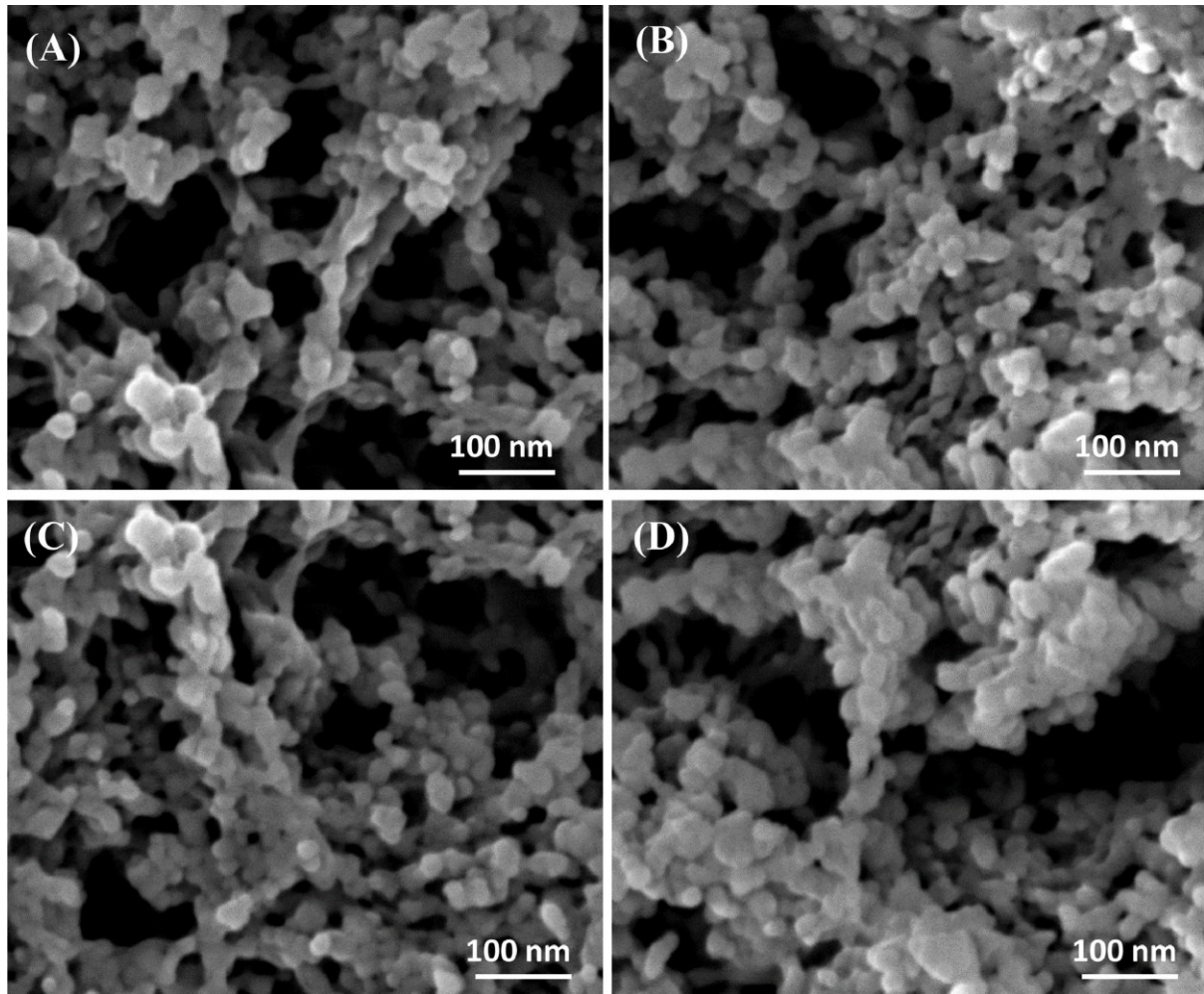
Fig. 2. Transmission electron microscopy images of (A, and B) S2 of NiHCF, and (C, and D) S2 of NiHCF annealed at 100 °C in air atmosphere.
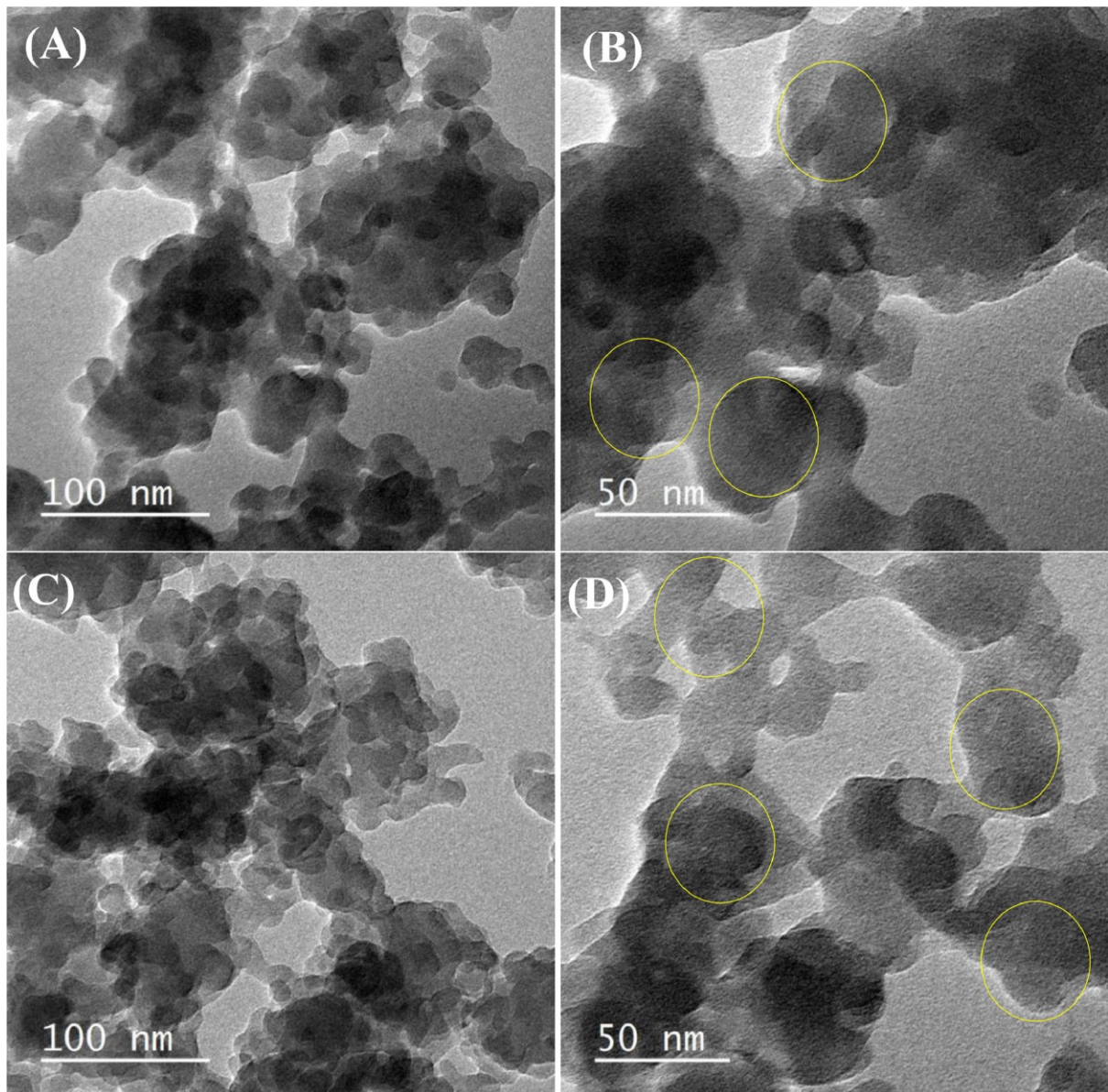
Fig. 3. (A) Thermal gravimetrical analysis of as-synthesized NiHCF (S2) in air and nitrogen atmospheres, (B) X-ray diffraction with scan speed 2° /min of as-synthesized NiHCF (S2) and NiHCF samples annealed in air and nitrogen atmospheres, (C) Fourier transform infrared spectroscopy and (D) Nitrogen adsorption/desorption isotherms of NiHCF analogs.
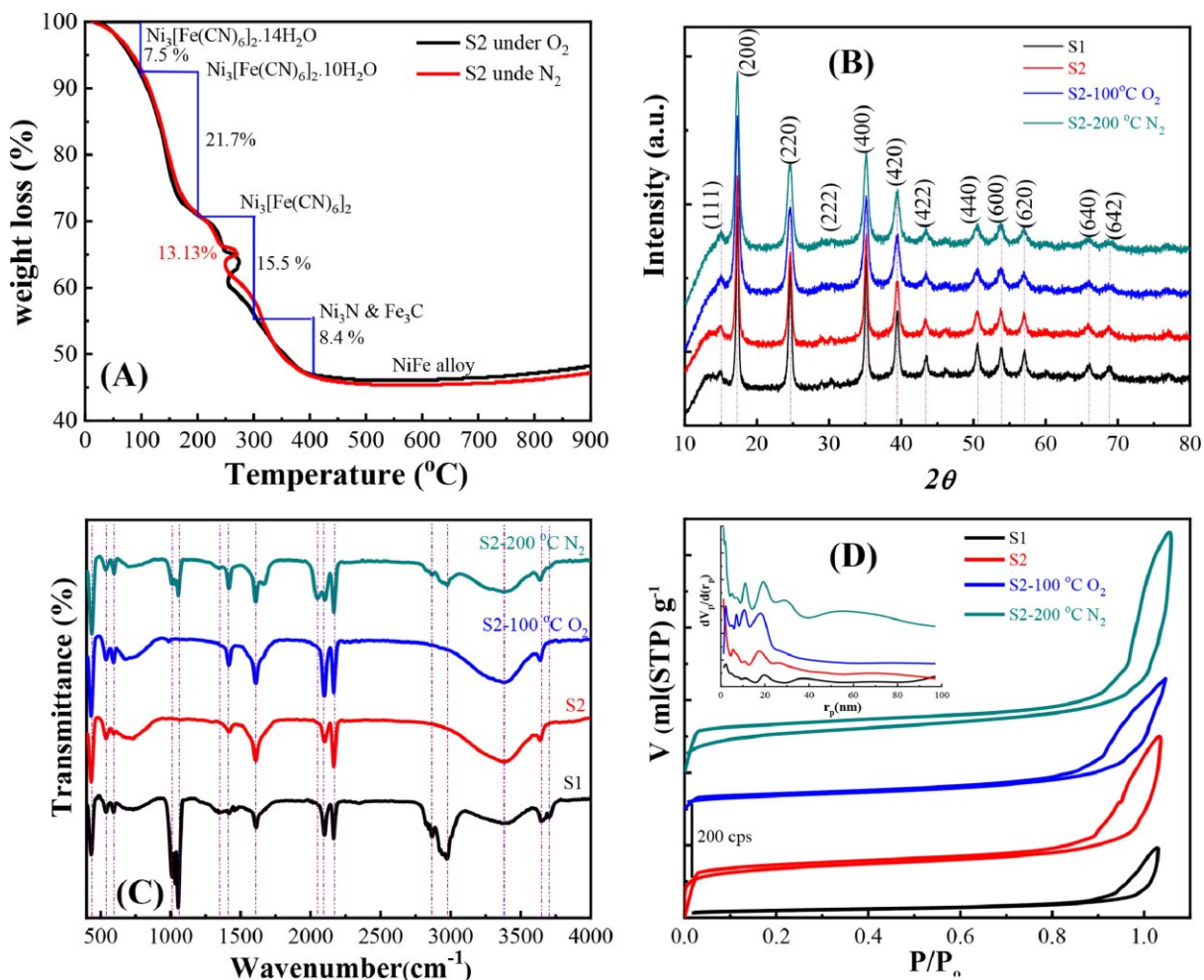
Fig. 3A shows the thermal gravimetric analysis of NiHCF from 30 to 900 °C in oxygen and nitrogen atmospheres at a heating rate of 10 °C min−1. Obvious weight loss regions are found in the temperature range from 50 °C to 400 °C. The weight loss is about 7.5% between 50–100 °C, which relates to loss of adsorbed physical water. Besides, the interstitial or coordinated water molecules remove from NiHCF crystal in the range of 100 °C to 200 °C with a weight loss of 21.7%, corresponding to a crystal structure of Ni3[Fe(CN)6]2•10H2O, as also proposed by XRD (Fig. 3B). The total water loss is about 29.2%. Then, anhydrous NiHCF is formed at 200 °C, accompanied by decomposition of metal-organic frameworks at 320 °C. The gradual loss of the hydrated and coordinated water might facilitate the diffusion of ions into the NiHCF 3D open frameworks [30].

The structural features of NiHCF and its analogues are investigated by wide-angle X-ray diffraction as shown in Fig. 3B. Well-resolved and distinctive diffraction peaks of NiHCF and its analogues are presented at 2θ of 15.01°, 17.3°, 24.54°, 29.1°, 30.64°, 35.1°, 39.41°, 43.4°, 50.65°, 53.89°, 57.13°, 66.08°, and 68.87° . These diffraction peaks can be indexed for (111), (200), (220), (311), (400), (420), (422), (440), (600), (620), (640) and (642), respectively, consistent with JCPDS no. 46–0906 for Ni3[Fe(CN)6]2•10H2O. The NiHCF and its analogues showed a cubic (F4−3 m) symmetry with a lattice constant of a = 10.22 Å. Furthermore, no changes in the diffraction patterns were observed through annealing at 100 °C in the air or even at 200 °C in nitrogen atmospheres, indicating the structural stability of NiHCF at relatively high temperatures.

To investigate the functional groups of NiHCF samples, the FTIR spectroscopy was performed. Two small absorption bands at 3708 and 3649 cm^{-1} were assigned to symmetric and asymmetric stretching of H_2O molecules, respectively. The broad absorption band at 3375 cm^{-1} is attributed to Osingle bondH stretching. These results indicate the presence of hydrated and coordinated water molecules in the NiHCF sample as shown in TGA. Another absorption band at 1610 cm^{-1} attributed to Osingle bondH bending [31]. The broad absorption bands at 2973–2865 cm^{-1} assign to −CH2 antisymmetric and symmetric stretching, respectively, indicating the presence of residual PVP. The absorption peaks at 2169, 2091 and 2050 cm−1 are attributed to Ctriple bondN bridging stretching. The free Ctriple bondN group usually exhibits a sharp stretching band at 2060 cm^{-1}. When CN group forms a complex with transition metals tends to act as σ donor and the complex depends upon the electronegativity, oxidation state and coordination number of the bonded metal. Thus, the absorption band at 2169 and 2091 cm−1 might be related to Ni(II)Ctriple bondN-Fe(II) and Ni(II)-Ctriple bondN-Fe(III) indicating the presence of Fe(II)/Fe(III) species in the NiHCF framework as also suggested previously [32,33]. It is

found the intensity of the absorption peak at 2091 cm−1 increases after the NiHCF is annealed at 100 °C, which confirms the oxidation of Fe(II) to Fe(III). PBAs are well-known materials that could bear $Fe(CN)_6$ or CN^- vacancies which allow alteration of electron transfer phenomena within the framework [18]. Interestingly, a new absorption band is observed at 2050 cm^{-1} if the S2 annealed at 200 °C under nitrogen atmosphere, which attributed to free C triple bond N group on the surface as shown by EDX analysis. Thus, control annealing of PBAs could represent different crystal vacancies or active sites within the NiHCF framework since the XRD have the same cubic crystal lattice (Fig. 3B). The small absorption bands at 1414 and 1346 cm^{-1} can be assigned to symmetric −COO−stretching and -CH deformation which regarding to residual citrate ions. The broad peak from 1003 cm^{-1} to 1061 cm^{-1} attribute to −C single bond C- stretching. The absorption bands at 591.5 and 434.6 cm^{-1} can be assigned to Fe-CN bending and Fe-CN stretching vibration modes, respectively. The absorption peak at 542.5 attributes to Ni-NC stretching.

Fig. 3D shows the nitrogen adsorption/desorption isotherms of NiHCF and its analogues and feature type IV isotherms with an H2-type hysteresis loop for the mesoporous framework. The specific surface areas are calculated to be 117.6, 452.9, 268.6, 390.8 m2g−1 for S1, S2, S2 annealed at 100 °C in an oxygen atmosphere and S2 annealed at 200 °C in a nitrogen atmosphere, respectively. The pore size distribution also is estimated using the BJH model as shown in inset Fig. 3D. We can see a multidirectional porous network with different pore sizes after annealing the sample (2) in air and nitrogen atmospheres. Such an open framework might exhibit variable affinity to store charges via intercalation for non-faradaic and redox active sites for faradaic processes. Therefore, the NiHCF and its analogues have been studied in different supporting electrolytes.

Electrochemical characteristics of NiHCF samples

The electrochemical behaviour of NiHCF and its analogues are studied by cyclic voltammetry and galvanostatic charge/discharge and electrochemical impedance spectroscopy techniques. Figs. 4 and S3 shows the cyclic voltammograms of as-synthesized NiHCF sample (S2) and sample (S1), respectively, in 0.1 M KCl, 0.1 M NaCl, 0.1 M KOH, and 0.1 M NaOH over a potential window of 0.0 to 1.5 V (vs. Ag/AgCl). The CVs are recorded after ten repetition cycles since the redox peak currents increases. For all supporting electrolytes, the height of peak current enhances with increasing the potential scan rates. Furthermore, linear correlations are found between peak current and the square root of scan rates indicating the diffusion-controlled process of reactive species at the electrode

surface (Fig. S4). We can see the oxidation peak potential shifts toward positive values with increases of the potential scan rate in the range of 20 −200 mV/s. The NiHCF samples represent quasi-reversible signals with peak separations (ΔEp) higher than 350 mV at a scan rate of 50 mV/s and increase up to 500 mV in NaOH and KOH. The peak current of NiHCF sample (S2) is higher than the sample (S1) which shows a promising energy storage capability. Therefore, sample (2) is selected for further investigations as energy storage platform. For NiHCF sample (2), the oxidation peak potentials are found at 0.90, 0.82, 1.08, and 1.028 V vs. Ag/AgCl in KCl, NaCl, KOH, and NaOH at 50 mV/s. It is well-known that a reactive couple of $[Fe(CN)_6]^{3-}/[Fe(CN)_6]^{4-}$ is stable in an alkaline medium and used also as an affective redox couple in 1 M KOH for nickel hydroxide/graphene supercapacitor [34,35]. The difference in the oxidation peak potential of NiHCF in NaCl and KCl solutions might be related to the size of hydrated cations that interact within the NiHCF open framework [25]. To investigate the possible electrochemical storage mechanism, we suggested that the oxidation peak currents of NiHCF (S2) in different supporting electrolytes obey the power-law relation with the potential scan rates as:

$$i = a\nu^b$$

where a, and b are adjustable constants. The value of b is equal to 0.5 for the current controlled by semi-infinite linear diffusion and value of 1 for the surface-controlled process. The value of b is calculated to be 0.61, 0.62, 0.48, 0.5 in KCl, NaCl, KOH, and NaOH indicating battery-type behaviours platforms. The concrete fraction of the diffusion and surface processes can be deduced through the equation suggested by Dunn's as follow [36], [37], [38].

$$i(V)/\nu^{1/2} = k_1\nu^{1/2} + k_2$$

where the surface-controlled part (k1v) and the diffusion-controlled part of k2v1/2 can be quantified as shown in Fig. S5. The fraction of surface- and diffusion-controlled contributions are 46.23% and 53.77% of the total stored charge in 0.1 M KCl. While, the fraction of surface- and diffusion-controlled contributions are 16.48% and 83.16% of the total stored charge in 0.1 M KOH. It is reported that NiHCF in aqueous electrolytes shows the activity of low-spin iron ion redox centre only and nickel atoms known at valence state (II) [39]. Therefore, this peak attributed to oxidation of Fe(II) that coordinated by cyanide groups via carbon atoms to Fe (III) and also cation extraction from NiHCF NaCl and KCl solutions in the reverse direction as follows:

$$Ni^{II}_3[Fe^{III}(CN)_6]_2 + 2A^+ + 2e^- \leftrightarrow A_2Ni^{II}_3[Fe^{II}(CN)_6]_2$$
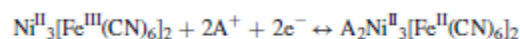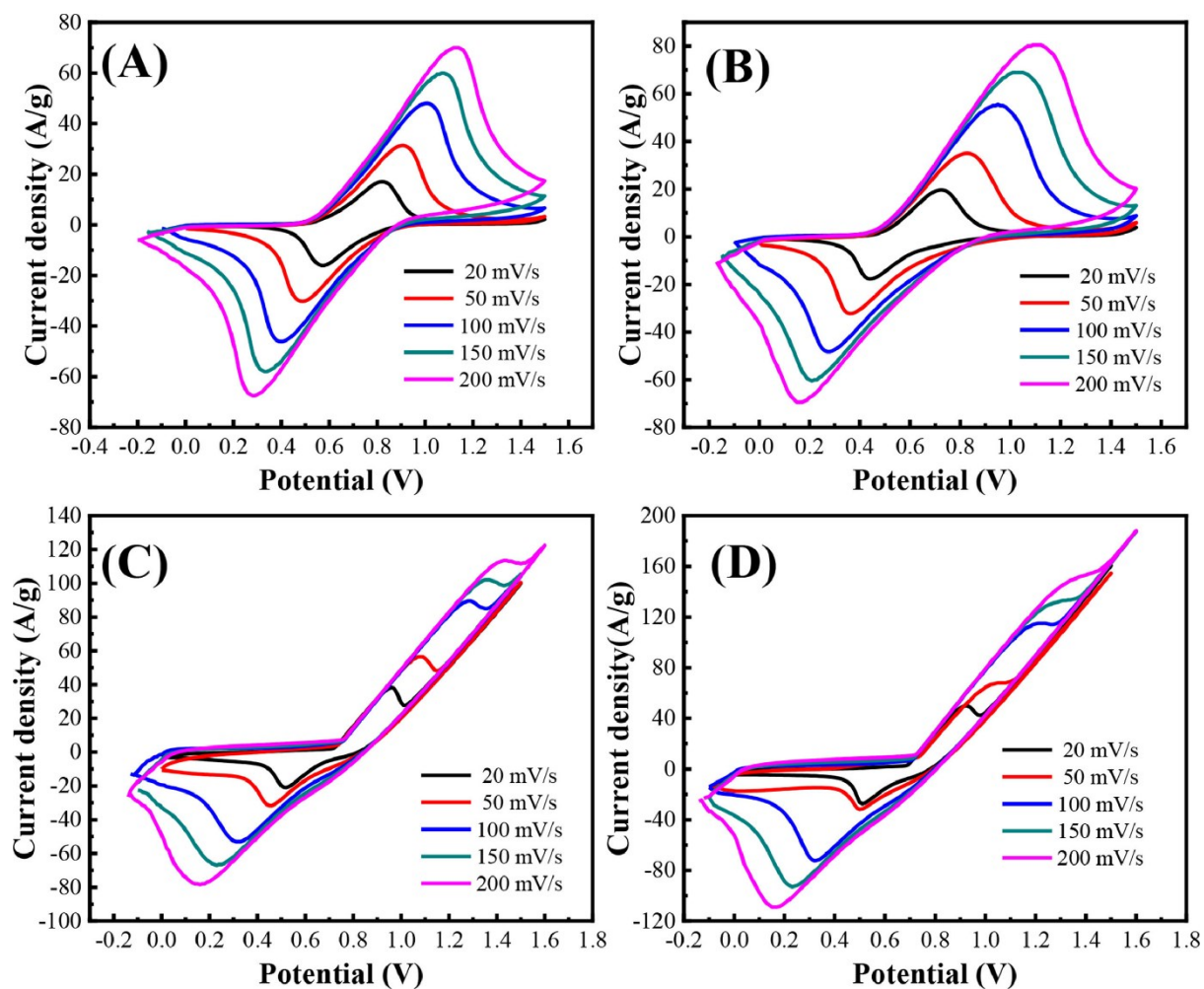
Fig. 4. (A) Cyclic voltammetric curves of as-synthesized NiHCF (S2) in (A) 0.1 M NaCl, (B) 0.1 M KCl, (C) 0.1 M NaOH, and (D) 0.1 M KOH at different scan rates.

On the other hand, the oxidation peak potential shifts more than 0.1 and 0.2 V vs. Ag/AgCl in KOH and NaOH solutions compared to KCl and NaCl, respectively. Indicating the formation of NiO(OH) or (Ni-Fe)O(OH) reactive species in KOH and NaOH solutions [18]. Thus, the peak currents are increased almost three times compared to KCl and NaCl. In the meantime, the cathodic peak at 0.45 V vs. Ag/AgCl at 50 mV/s is observed showing the reverse processes. Subsequently, the high current signal in the basic medium might imply a superior integrated energy storage system via faradaic and non-faradaic processes similar to battery-like metal oxide electrode [7]. The specific capacitance (Cs) is calculated to be 210, 255, 409, and 356 F/g at 50 mV/s in 0.1 M NaCl, 0.1 M KCl, 0.1 M KOH, and 0.1 M NaOH, respectively. The high surface area of NiHCF revealed a promising specific capacitance higher than that reported previously even by a combination of MnO2/NiHCF dual-layer composites [40].

Next, we turn to perform galvanostatic charge/discharge of NiHCF samples in different supporting electrolytes at a current density of 5 A/g in the potential range from 0.0 to 0.8 V vs. Ag/AgCl as shown in Fig. S6. The NiHCF samples were prepared by different ratios of Ni(II) and KHCF labelled as S1, S2 and S3. Amongst the NiHCF samples, S2 shows superior electrochemical performance as energy storage electrodes. To runderstand why sample (3) gives a low storage capability, the specific surface area was measured and found to be 204 m2/g. Thus, the addition of twice concentration of nickel ions to PHCF causes a rapid growth of NiHCF with a low surface area. Thus, the storage capability of NiHCF is mainly controlled by a specific surface area (SBET). The specific capacitance of NiHCF (S2) was calculated to be 197.5, 139.35, 356.25, and 406.25 F/g in 0.1 M KCl, 0.1 M NaCl, 0.1 M NaOH and 0.1 M KOH respectively at the current density of 5 A/g in a potential window of 0.0–0.8 V vs. Ag/AgCl. While the SPEs used as current collector and does not show any capacity as shown in Fig. S7. The effect of supporting electrolyte concentrations upon the storage capability of NiHCF (S2) was also studied as shown in Fig. S8. The cyclic voltammogram of NiHCF in KCl did not change by increasing the concentration of KCl up to 10-times. It was found the evolution of chorine was occurred at lower potential by increasing the concentration of KCl. Since the cyclic voltammogram related to [Fe(CN)6]3-/4- lies before the evolution of chlorine gas, the galvanostatic charge/discharge curve did not affect [41]. However, when the concentration of KOH increases to 1.0 M, the working applied voltage range is decreased to 0.6 V which might be due to oxygen evolution process and the discharge time is slightly increased which reveals a specific capacitance of 575 F/g at 5 A/g.

Fig. 5 shows a galvanostatic charge/discharge curve of NiHCF in 0.1 M KOH at different discharge current densities. The specific capacitance is calculated for discharge arm and found to be 412, 410,

408, and 406 F/g at current densities of 2, 3, 4, and 5 A/g, respectively. Further, the coulombic efficiency (η) was calculated to by higher than 80%. Superior capability rate of NiHCF (S2) is reported since the specific capacitance is retained 98.5% during cycling at a discharge rate of 5 A/g. The stability of NiHCF is studied by performing charge/discharge cycling between 0.0 to 0.9 V vs. Ag/AgCl at a current density of 5 A/g. The NiHCF (S2) shows good cycling stability and the capacitance increases to 500 F/g after 100 cycles, and then decreases again to its original value of 410 F/g after 1000 cycles (Fig. 7B). The NiHCF as battery-like materials, the redox reaction carried out in inner space and intercalation/de-intercalation of ions might cause fast fading of capacitance values [40]. However, the as-synthesized NiHCF manifests excellent energy storage capabilities even at high current densities compared with previously reported studies (Table 1 and Fig. S14). Interestingly, the presence of PVP and SC in the reaction conditions retard nucleation growth and thus minimize the [Fe(CN)6] vacancies and coordinated water in PBA frameworks as described by ICP-OES and EDX analyses. As a result, the value of the specific capacitance is significantly enhanced and showed excellent cycling stability and capability rates. Further, the effect of NiHCF particle size on the storage performance was also investigated. The NiHCF samples (S4 and S5) with different particle sizes were prepared by variation of citrate ion ratios as previously reported [27] and the result is shown in Fig. S9. The S2 of NiHCF that synthesized using 150 mg of citrate showed a low particle size and high specific capacitance. This observation might due to increase of active sites density for faradaic process in alkaline medium as the faradic process contributes more than 83% of the total capacitance.

Fig. 5. (A) Galvanostatic discharge curves of as-synthesized NiHCF (S2) in 0. 1 M KOH at different discharge current, and (B) Galvanostatic charge /discharge curve of as-synthesized NiHCF (S2) at 5 A/g for 40 cycles in 0.1 M KOH.
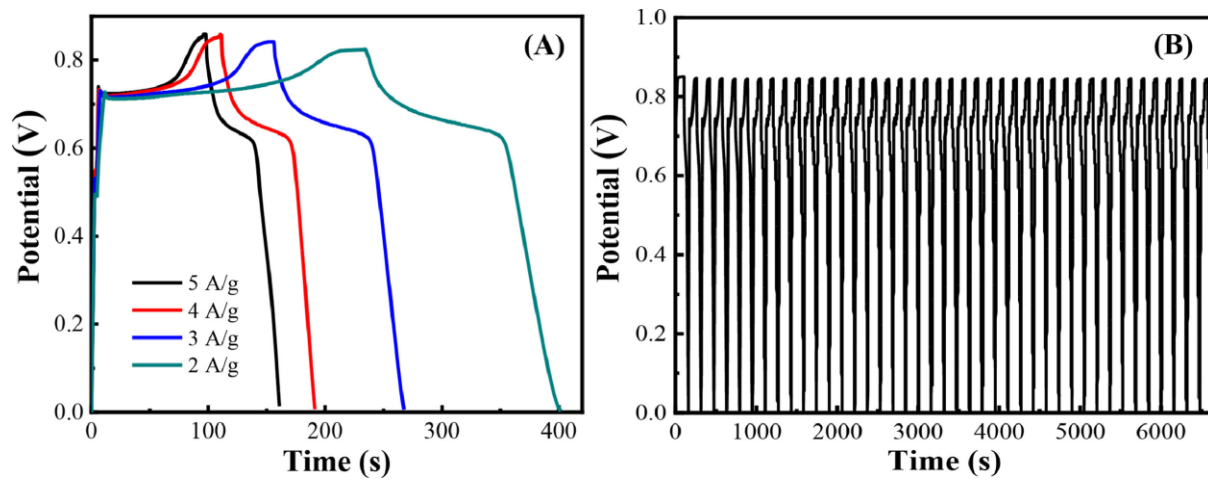
Table 1. Comparison of synthesized NiHCF with previously reported electrodes.

Active electrode	Current density	Specific capacitance (F/g)	Electrolyte	Refs.
$Ni_3[Fe(CN)_6].2H_2O/$ stainless steel grids	0.2 A/g	574.7	1 M KNO_3	[25]
Ni [Fe(CN)$_6$]/ GCE	1 A/g	149	1 M $NaClO_4$	[43]
NaCo[Fe (CN)$_6$] / GCE	1 A/g	295	1 M Na_2SO_4	[43]
$Mn_3[Fe(CN)_6]_2 \cdot xH_2O/$ Nickel foam		238	0.5 M Na_2SO_4	[44]
PANI/$Ni_3[Fe(CN)_6]_2$ /sCNTs	2 mA/cm^2	430.77	0.5 M H_2SO_4 + 0.5 M KNO_3	[45]
$Co_3[Fe(CN)_6]_2$ /Nickel foam	1 A/g	441	1 M Na_2SO_4	[46]
$Ni_3[Fe(CN)_6]_2@MnO_2/$ Nickel foam	1 A/g	199.6	1 M Na_2SO_4	[40]
$Co_3[Fe(CN)_6]_2$ /Nickel foam	1A/g	284	0.5 M Na_2SO_4	[24]
$Co_3[Fe(CN)_6]_2$/Nickel foam	0.5A/g	288	0.5 M Na_2SO_4	[47]
$Ni_3[Fe(CN)_6]_2/$ CTAB/rGO/Nickel foam	0.2A/g	415	0.5 M Na_2SO_4	[48]
$Ni_3[Fe(CN)_6]_2$ /stainless steel grids	0.2 A/g	547.5	1 M KNO_3	[49]
$Co_3[Fe(CN)_6]_2/$ stainless steel grids	0.2 A/g	261.56	1 M KNO_3	[49]
$Fe_3[Fe(CN)_6]_2/$ stainless steel grids	0.2 A/g	425	1 M KNO_3	[49]
NiHCF/SPEs	5 A/g	406	0.1 M KOH	This work
NiHCF_100 °C $O_2/$ SPEs	5 A/g	546	0.1 M KOH	This work
NiHCF_200 °C $N_2/$ SPEs	5 A/g	342	0.1 M KOH	This work

Next, attention was turned to investigate the effect of annealing temperatures on the energy storage capability. Fig. S10 shows cyclic voltammetry curves of annealed NiHCF (S2) in oxygen and nitrogen atmospheres at 100, 200 and 300 °C in 0.1 M KOH at scan rate 50 mV/s in the potential range of 0.0 to 1.4 V vs. Ag/AgCl. In an oxygen atmosphere, the oxidation peak potential shifts to more positive potentials. Besides, the oxidation peak current increases if NiHCF is annealed at 100 °C, reduces at 200 °C and disappears at 300 °C due to decomposition of the framework at a relatively high temperature as described in TGA analysis. In a nitrogen atmosphere, the oxidation peak potential shifts slightly to less positive values. The oxidation peak current enhances if the NiHCF is annealed at 200 °C. The galvanostatic discharge curves of NiHCF annealed in oxygen and nitrogen atmospheres showed a similar trend corresponding to their cyclic voltammograms. The specific capacitances are calculated at a current density of 5 A/g and found to be 546, 322, and 29 F/g of NiHCF annealed in an oxygen atmosphere at 100, 200, and 300 °C, respectively. Meanwhile, the specific capacitances of NiHCF annealed in a nitrogen atmosphere at 100, 200, and 300 °C are calculated to be 300, 342, and 164 F/g, respectively. The specific capacitance of NiHCF annealed in oxygen at 100 °C is higher than as-prepared NiHCF and NiHCF annealed in nitrogen in 0.1 M KOH by almost 35% and 60%, respectively. This result indicates that the vacancy of $Fe(CN)_6$ and/or CN groups might be possible after heating at 100 °C in oxygen atmosphere inside NiHCF framework which boosts the diffusion of OH− and easily formation of (Ni-Fe)O(OH) layers at the surface as shown in EDX analysis [18]. While, the $Fe(CN)_6$ vacancies decreases in the presence of nitrogen gas even after annealing at higher temperatures although it induces large surface area as shown in nitrogen adsorption/desorption isotherms (Fig. 3D). The significant reduction of the specific capacitance values was observed which might be due to formation of NiO(OH) species on the surface. It is reported that the nitrogen gas prevents the oxidation of Fe(II) to Fe (III) in NiHCF framework (as shown in FTIR (Fig. 3C)) and significantly enhances the intercalation with K+ ions within NiHCF [42]. The intercalation of K+ within the NiHCF crystal might compete the diffusion of OH− ions and reduce the faradaic reaction as shown in the electrochemical impedance spectra (EIS) of NiHCF samples (Fig. S11).

Fig. 6 shows cyclic voltammetry curves and galvanostatic discharge curves of annealed NiHCF at different scan rates and current densities in 0.1 M KOH. The annealed NiHCF samples show similar CV curves with quasi-reversible signals consistent with as-synthesized NiHCF in 0.1 M KOH. With increasing the potential scan rates, the oxidation peak potential shifted to more positive values and potential peak separation is increased. The oxidation peak current increases with increasing potential scan rates. Further, the peak height correlated linearly with the square root of scan rates, indicating a mass-transfer-controlled process of the reactive species at the flexible SPEs. The galvanostatic

charge/discharge curves of thermally treated NiHCF performed at different current densities as shown in Fig. 6 (B and D). We can see that the voltage plateaus are around 0.75- 0.65 V vs. Ag/AgCl corresponding to faradaic redox reaction observed in the CV voltammogram, confirming the pseudo-capacitive behaviour. The specific capacitances of NiHCF annealed in the oxygen atmosphere are calculated to be 471, 490, 516, 550, and 546 F/g at 1, 2, 3, 4, and 5 A/g, respectively. Meanwhile, the specific capacitances of NiHCF annealed in the nitrogen atmosphere are calculated to be 310, 320, 340, 342, and 342 F/g at 1, 2, 3, 4, and 5 A/g, respectively. Interestingly, the NiHCF samples annealed at oxygen and nitrogen atmospheres showed high capability rates. The specific capacitance of NiHCF annealed at 100 °C in oxygen revealed higher specific capacitance than the as-synthesized NiHCF and annealed under nitrogen atmosphere. Fig. 7 represents the cycling stability and coulombic efficiency of NiHCF samples over 1000 cycles in 0.1 M KOH at a current density of 5 A/g. The as-synthesized and thermally treated NiHCF samples revealed high cycling stability higher than 92% after 1000 cycles. Although the NiHCF annealed in nitrogen atmosphere showed lower specific capacitance, it shows promising cycling stability with retention of 100% after 1000 cycles. The coulombic efficiency provides clear evidence for the reversibility of the active materials at the electrode surface. For NiHCF (S2), the coulombic efficiency decreases from 95% to 85% during 1000 cycles. The coulombic efficiency decreases from 92% to 84% for NiHCF sample (2) annealed at 100 °C in oxygen. Meanwhile, the coulombic efficiency increases from 88% to 90% for NiHCF sample (2) annealed at 200 °C in nitrogen. These results indicate the reversibility of the electrode reaction stabilized and improved after annealing in nitrogen at 200 °C. To check the flexibility of screen-printed electrodes, the electrode was twisted in different directions and then the specific capacitance was measured in each ten bending cycles. After hundred bending cycles, the NiHCF/SPE maintained more than 85% of its original specific capacitance value as shown in Fig. S12.

Fig. 6. Cyclic voltammetric curves of NiHCF (S2) (A) annealed at 100 °C in air atmosphere and (C) Annealed at 200 °C in nitrogen atmosphere at different scan rates, and galvanostatic discharge curves of NiHCF sample (2) (B) Annealed at 100 °C in oxygen atmosphere and (D) Annealed at 200 °C in nitrogen atmosphere in 0.1 M KOH at different discharge currents.
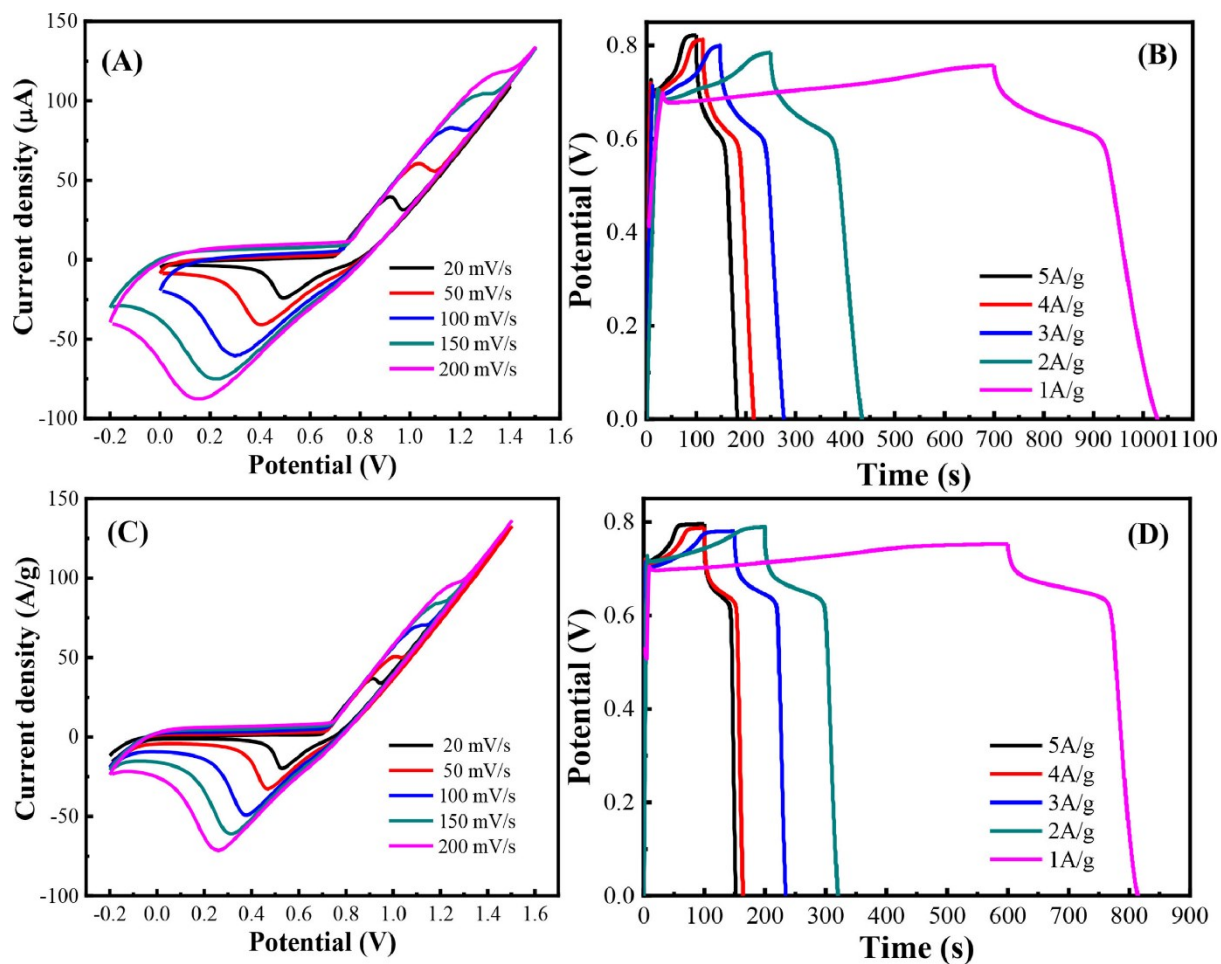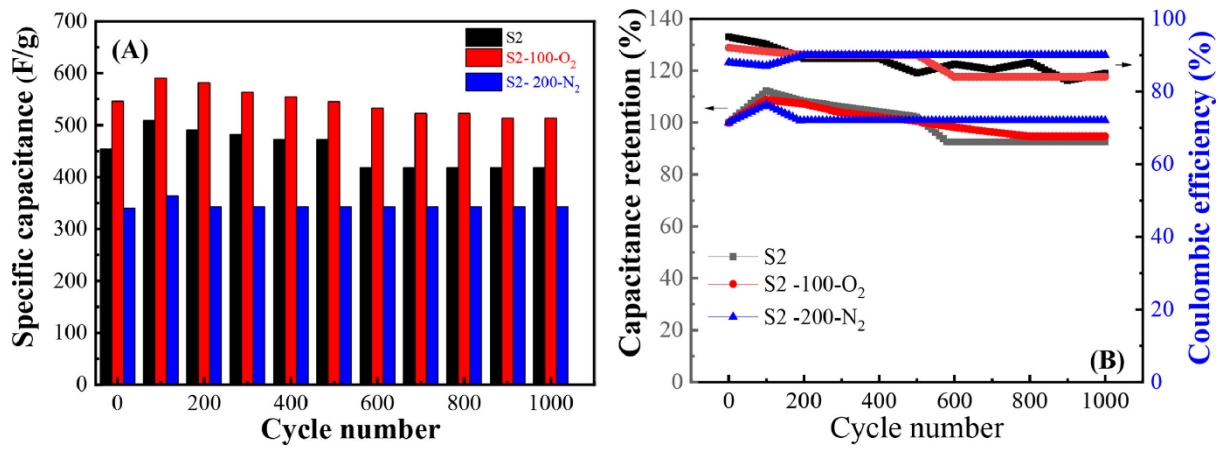
Fig. 7. (A) Calculated specific capacitance and (B) Retention percentage for NiHCF samples over 1000 cycles.

Figs. 8 and S13 shows the cyclic voltammetry curves and galvanostatic charge/discharge curves of annealed NiHCF (S2) in oxygen at 100 °C and nitrogen at 200 °C in 0.1 M KOH using a two-electrode cell configurations. Firstly, the cyclic voltammograms were recorded after ten CV cycles to ensure stabilization of CV signals. Then, the capability of NiHCF/SPE electrode was explored as positive electrode after connection with bare SPE, carbon black (CB)/SPE and NiHCF/SPE as negative one. It was found the commercially available SPE could be used efficiently (Fig. S13B). The cyclic voltammograms measured at different scan rates in the range 20 to 200 mV/s at the potential range of −0.2 to 1.6 V. A quasi-reversible signal is observed similar to a three-electrode cell configuration for the NiHCF samples treated in oxygen and nitrogen. With increasing the potential scan rates, the oxidation peak potential shifts toward more positive values and the reduction peak potential shifts to more negative values. Further, the peak height is also increased. The peak currents increase linearly with the square root of the scan rate. The galvanostatic charge/discharge curves of thermally treated NiHCF were carried out at different current densities (Fig. 8 (B and D)). We can see that, the voltage plateaus are around 0.5- 0.4 V. The specific capacitances of NiHCF sample (2) annealed in oxygen are calculated to be 570, 572, 594, 608, and 610 F/g at 1, 2, 3, 4, and 5 A/g, respectively. Meanwhile, the voltage plateaus are around 0.5- 0.45 V for NiHCF sample (2) annealed in nitrogen and the specific capacitances are calculated to be 420, 408, 426, 423, and 426 F/g at 1, 2, 3, 4, and 5 A/g, respectively. Fig. S14 shows the Ragone plot of the as-synthesized NiHCF (S2), after treatment at 100 °C in oxygen and 200 °C in nitrogen in 0.1 M KOH. Interestingly, the as-synthesized NiHCF (S2) or after treatment in oxygen and nitrogen offer excellent capability rates and cycling stabilities for supercabattery devices. Since, the supercabattery device combining the functions of a supercapacitor and a battery, the NiHCF/SPEs behave battery-like electrode in KCl and pseudocapacitive electrode in KOH. Thus, it can be used efficiently for practical applications.

Fig. 8. Cyclic voltammetric curves of NiHCF (S2) (A) annealed at 100 °C in air atmosphere and (C) Annealed at 200 °C in nitrogen atmosphere at different scan rates, and galvanostatic discharge curves of NiHCF sample (2) (B) annealed at 100 °C in air atmosphere and (D) Annealed at 200 °C in nitrogen atmosphere in 0.1 M KOH at different discharge currents connected in a two-electrode system.
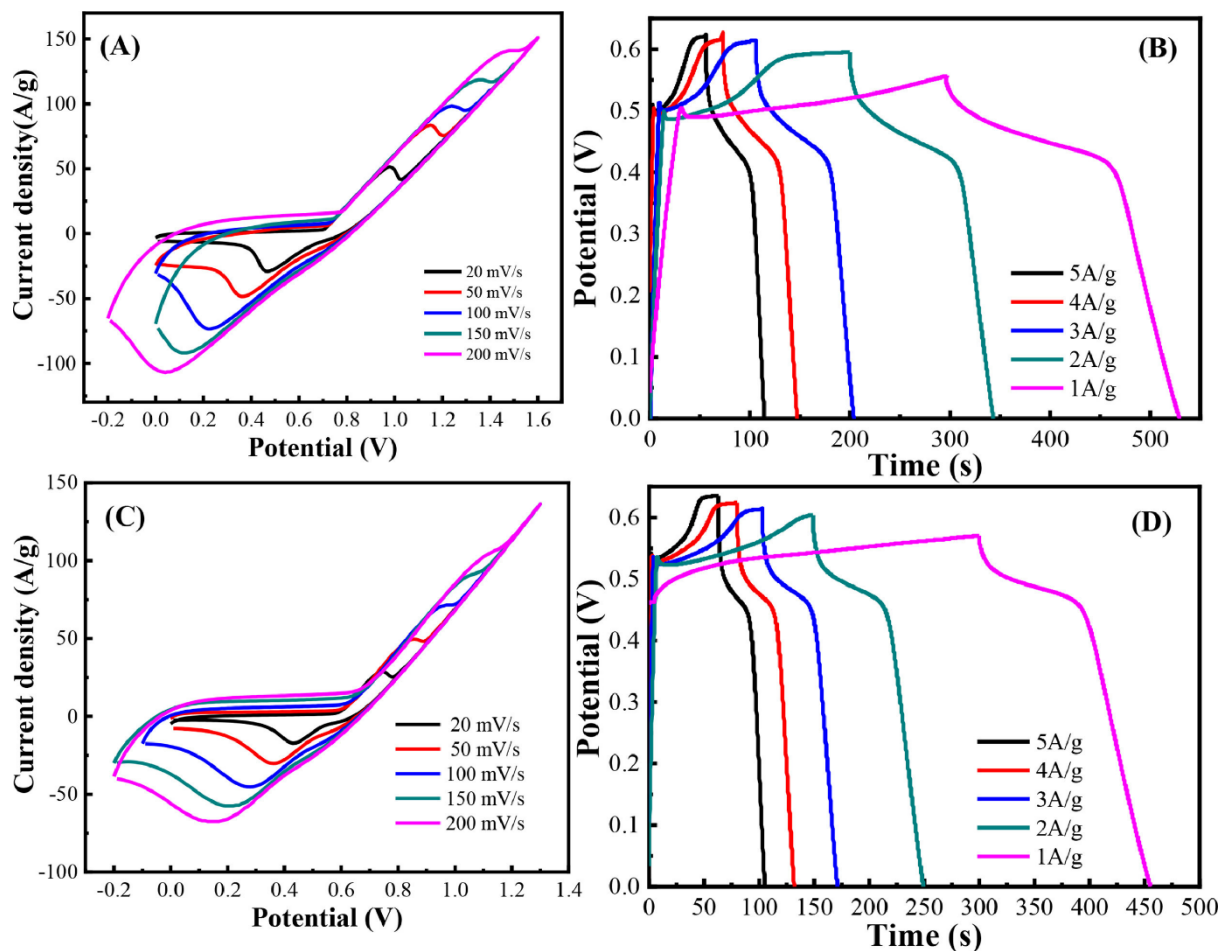
Conclusions

Nickel hexacyanoferrate (NiHCF) nanoparticles with an average size of 35 nm and specific surface area (SBET) of 452.9 m2/g have been are prepared by simple precipitation method upon screen-printed graphite macroelectrodes for supercapacitor applications. The NiHCF/SPEs studied in different supporting electrolytes KCl, NaCl, NaOH and KOH showed a specific capacitance of 197.5, 139.35, 356.25, and 406.25 F/g, respectively at a current density of 5 A/g. After annealing the NiHCF at 100, 200, and 300 °C in oxygen and nitrogen atmospheres, samples treated at 100 °C in oxygen and 200 °C in nitrogen revealed a specific capacitance of 546 and 342 F/g, respectively. Meanwhile, they showed 610 and 426 F/g in the two-electrode system. All the NiHCF samples represented superior capability and cycling stability with excellent columbic efficiencies, which offer low cost and promising energy storage devices.

CRediT authorship contribution statement

Mohamed Khairy: Conceptualization, Methodology, Investigation, Validation, Data curation, Writing – original draft. Khaled G. Mahmoud: Methodology, Formal analysis, Writing – original draft. Farouk A. Rashwan: Supervision, Resources. Hussein M. El-Sagher: Supervision, Resources. Craig E. Banks: Writing – review & editing.

Declaration of Competing Interest

The authors declare that they have no known competing financial interests or personal relationships that could have appeared to influence the work reported in this paper.

Appendix. Supplementary materials

Download : Download Word document (2MB)

References

[1] P. Simon, Y. Gogotsi, Perspectives for electrochemical capacitors and related devices

Nat. Mater., 19 (11) (2020), pp. 1151-1163,

[2] Y. Lin, L. Zhang, Y. Xiong, T. Wei, Z. Fan, Toward the design of high-performance supercapacitors by prussian blue, its analogues and their derivatives, Energy Environ. Mater., 3 (3) (2020), pp. 323-345

[3] H. Lv, Q. Pan, Y. Song, X.X. Liu, T. Liu, A review on nano-/microstructured materials constructed by electrochemical technologies for supercapacitors, Nano Micro Lett., 12 (2020), pp. 1-56

[4] E.S. Goda, S. Lee, M. Sohail, K.R. Yoon, Prussian blue and its analogues as advanced supercapacitor electrodes, J. Energy Chem., 50 (2020), pp. 206-229

[5] Y. Zhang, S.J. Park, Incorporation of RuO_2 into charcoal-derived carbon with controllable microporosity by CO_2 activation for high-performance supercapacitor, Carbon N Y, 122 (2017), pp. 287-297

[6] M. Khairy, H.A. Ayoub, C.E. Banks, Large-scale production of $CdO/Cd (OH)_2$ nanocomposites for non-enzyme sensing and supercapacitor applications, RSC Adv., 8 (2) (2018), pp. 921-930

[7] M. Khairy, S.A. El-Safty, Nanosized rambutan-like nickel oxides as electrochemical sensor and pseudocapacitor, Sens. Actuators B Chem., 193 (2014), pp. 644-652

[8] Y. He, P. Zhang, F. Wang, L. Wang, Y. Su, F. Zhang, X. Zhuang, X. Feng, Vacancy modification of Prussian-blue nano-thin films for high energy-density micro-supercapacitors with ultralow RC time constant, Nano Energy, 60 (2019), pp. 8-16

[9] J. Cherusseri, N. Choudhary, K.S. Kumar, Y. Jung, J. Thomas, Recent trends in transition metal dichalcogenide based supercapacitor electrodes, Nanoscale Horizons, 4 (4) (2019), pp. 840-858

[10] K.S. Kumar, N. Choudhary, Y. Jung, J. Thomas, Recent advances in two-dimensional nanomaterials for supercapacitor electrode applications, ACS Energy Lett., 3 (2) (2018), pp. 482-495

[11] J.S. Shayeh, S.O.R. Siadat, M. Sadeghnia, K. Niknam, M. Rezaei, N. Aghamohammadi, Advanced studies of coupled conductive polymer/metal oxide nano wire composite as an efficient supercapacitor by common and fast fourier electrochemical methods, J. Mol. Liq., 220 (2016), pp. 489-494

[12] L. Samain, F. Grandjean, G.J. Long, P. Martinetto, P. Bordet, D. Strivay, Relationship between the synthesis of Prussian blue pigments, their color, physical properties, and their behavior in paint layers, J. Phys. Chem. C, 117 (19) (2013), pp. 9693-9712

[13] M. Shokouhimehr, E.S. Soehnlen, J. Hao, M. Griswold, C. Flask, X. Fan, J.P. Basilion, S. Basu, S.D. Huang, Dual purpose Prussian blue nanoparticles for cellular imaging and drug delivery: a new generation of T 1-weighted MRI contrast and small molecule delivery agents, J. Mater. Chem., 20 (25) (2010), pp. 5251-5259

[14] C.R. Patra, Prussian blue nanoparticles and their analogues for application to cancer theranostics

Future Med. (2016)

[15] S.C. Jang, Y. Haldorai, G.W. Lee, S.K. Hwang, Y.K. Han, C. Roh, Y.S. Huh, Porous three-dimensional graphene foam/Prussian blue composite for efficient removal of radioactive 137 Cs, Sci. Rep., 5 (1) (2015), pp. 1-10

[16] M.A. Komkova, E.E. Karyakina, A.A. Karyakin, Noiseless performance of prussian blue based (Bio) sensors through power generation, Anal. Chem., 89 (12) (2017), pp. 6290-6294

[17] S.A. Patil, S. Cho, Y. Jo, N.K. Shrestha, H. Kim, H. Im, Bimetallic Ni-Co@ hexacyano nano-frameworks anchored on carbon nanotubes for highly efficient overall water splitting and urea decontamination, Chem. Eng. J. (2021), Article 130773

[18] Z.Y. Yu, Y. Duan, J.D. Liu, Y. Chen, X.K. Liu, W. Liu, T. Ma, Y. Li, X.S. Zheng, T. Yao, Unconventional CN vacancies suppress iron-leaching in Prussian blue analogue pre-catalyst for boosted oxygen evolution catalysis, Nat. Commun., 10 (1) (2019), pp. 1-9

[19] X. Wu, M. Shao, C. Wu, J. Qian, Y. Cao, X. Ai, H. Yang, Low defect FeFe (CN) 6 framework as stable host material for high performance Li-ion batteries, ACS Appl. Mater. Interfaces, 8 (36) (2016), pp. 23706-23712

[20] L. Li, P. Nie, Y. Chen, J. Wang, Novel acetic acid induced Na-rich Prussian blue nanocubes with iron defects as cathodes for sodium ion batteries, J. Mater. Chem. A, 7 (19) (2019), pp. 12134-12144

[21] M. Okubo, D. Asakura, Y. Mizuno, J.D. Kim, T. Mizokawa, T. Kudo, I. Honma, Switching redox-active sites by valence tautomerism in prussian blue analogues a x Mn y [Fe (CN)6]• n H2O (A: K, Rb): robust frameworks for reversible Li storage, J. Phys. Chem. Lett., 1 (14) (2010), pp. 2063-2071

[22] Y. Yue, A.J. Binder, B. Guo, Z. Zhang, Z.A. Qiao, C. Tian, S. Dai, Mesoporous prussian blue analogues: template-free synthesis and sodium-ion battery applications, Angew. Chem. Int. Ed., 53 (12) (2014), pp. 3134-3137

[23] W. Zhang, Y. Zhao, V. Malgras, Q. Ji, D. Jiang, R. Qi, K. Ariga, Y. Yamauchi, J. Liu, J.S. Jiang, Synthesis of monocrystalline nanoframes of prussian blue analogues by controlled preferential etching, Angew. Chem. Int. Ed., 55 (29) (2016), pp. 8228-8234

[24] X. Yin, H. Li, H. Wang, Z. Zhang, R. Yuan, J. Lu, Q. Song, J.G. Wang, L. Zhang, Q. Fu, Self-templating synthesis of cobalt hexacyanoferrate hollow structures with superior performance for Na-ion hybrid supercapacitors, ACS Appl. Mater. Interfaces, 10 (35) (2018), pp. 29496-29504

[25] J. Chen, K. Huang, S. Liu, X. Hu, Electrochemical supercapacitor behavior of $Ni_3(Fe(CN)_6)_2(H_2O)$ nanoparticles, J. Power Sources, 186 (2) (2009), pp. 565-569

[26] J. Song, L. Wang, Y. Lu, J. Liu, B. Guo, P. Xiao, J.-J. Lee, X.-Q. Yang, G. Henkelman, J.B. Goodenough

Removal of interstitial H_2O in hexacyanometallates for a superior cathode of a sodium-ion battery

J. Am. Chem. Soc., 137 (7) (2015), pp. 2658-2664

[27] Y.D. Chiang, M. Hu, Y. Kamachi, S. Ishihara, K. Takai, Y. Tsujimoto, K. Ariga, K.C.W. Wu, Y. Yamauchi

Rational design and synthesis of cyano-bridged coordination polymers with precise control of particle size from 20 to 500 nm, Eur. J. Inorg. Chem., 2013 (18) (2013), pp. 3141-3145

[28] M. Khairy, C.E. Banks, A screen-printed electrochemical sensing platform surface modified with nanostructured ytterbium oxide nanoplates facilitating the electroanalytical sensing of the analgesic drugs acetaminophen and tramadol, Microchim. Acta, 187 (2) (2020), pp. 1-10

[29] B.G. Mahmoud, M. Khairy, F.A. Rashwan, C.E. Banks, Simultaneous voltammetric determination of acetaminophen and isoniazid (hepatotoxicity-related drugs) utilizing bismuth oxide nanorod modified screen-printed electrochemical sensing platforms, Anal. Chem., 89 (3) (2017), pp. 2170-2178

[30] K. Singh, L. Zhang, H. Zuilhof, L. de Smet, Water desalination with nickel hexacyanoferrate electrodes in capacitive deionization: experiment, model and comparison with carbon, Desalination, 496 (2020), Article 114647

[31] B.M. Cullum, T. Vo-Dinh, Sample collection and preparation of liquid and solids, Handb. Spectrosc., 2 (2003), p. 1

[32] X. He, L. Tian, M. Qiao, J. Zhang, W. Geng, Q. Zhang, A novel highly crystalline Fe4(Fe (CN)6)3 concave cube anode material for Li-ion batteries with high capacity and long life, J. Mater. Chem. A, 7 (18) (2019), pp. 11478-11486

[33] J. Li, L. He, J. Jiang, Z. Xu, M. Liu, X. Liu, H. Tong, Z. Liu, D. Qian, Facile syntheses of bimetallic Prussian blue analogues (KxM [Fe (CN)6] nH2O, M= Ni, Co, and Mn) for electrochemical determination of toxic 2-nitrophenol, Electrochim. Acta, 353 (2020), Article 136579

[34] P. Marzak, J. Yun, A. Dorsel, A. Kriele, R. Gilles, O. Schneider, A.S. Bandarenka, Electrodeposited Na2Ni [Fe (CN)6] thin-film cathodes exposed to simulated aqueous Na-ion battery conditions, J. Phys. Chem.y C, 122 (16) (2018), pp. 8760-8768

[35] P. Sirisinudomkit, P. Iamprasertkun, A. Krittayavathananon, T. Pettong, P. Dittanet, P. Kidkhunthod, M. Sawangphruk, Hybrid energy storage of battery-type nickel hydroxide and supercapacitor-type graphene: redox additive and charge storage mechanism, Sustain. Energy Fuels, 1 (2) (2017), pp. 275-279

[36] K. Wang, Q. Li, Z. Ren, C. Li, Y. Chu, Z. Wang, M. Zhang, H. Wu, Q. Zhang, 2D metal–organic frameworks (MOFs) for high-performance BatCap hybrid devices, Small, 16 (30) (2020), Article 2001987

[37] K. Wang, R. Bi, M. Huang, B. Lv, H. Wang, C. Li, H. Wu, Q. Zhang, Porous cobalt metal–organic frameworks as active elements in battery–supercapacitor hybrid devices, Inorg. Chem., 59 (10) (2020), pp. 6808-6814

[38] V. Augustyn, J. Come, M.A. Lowe, J.W. Kim, P.L. Taberna, S.H. Tolbert, H.D. Abruña, P. Simon, B. Dunn, High-rate electrochemical energy storage through Li+ intercalation pseudocapacitance, Nat. Mater., 12 (6) (2013), pp. 518-522

[39] A. Lisowska-Oleksiak, A.P. Nowak, Metal hexacyanoferrate network synthesized inside polymer matrix for electrochemical capacitors, J. Power Sources, 173 (2) (2007), pp. 829-836

[40] Y. Wang, Q. Chen, Dual-layer-structured nickel hexacyanoferrate/MnO2 composite as a high-energy supercapacitive material based on the complementarity and interlayer concentration enhancement effect, ACS Appl. Mater. Interfaces, 6 (9) (2014), pp. 6196-6201

[41] P. Díaz, Z. González, R. Santamaría, M. Granda, R. Menéndez, C. Blanco, Enhancing energy density of carbon-based supercapacitors using Prussian Blue modified positive electrodes, Electrochim. Acta, 212 (2016), pp. 848-855

[42] Y. You, X. Yu, Y. Yin, K.W. Nam, Y.G. Guo, Sodium iron hexacyanoferrate with high Na content as a Na-rich cathode material for Na-ion batteries, Nano Res., 8 (1) (2015), pp. 117-128

[43] Y. Yue, Z. Zhang, A.J. Binder, J. Chen, X. Jin, S.H. Overbury, S. Dai, Hierarchically superstructured prussian blue analogues: spontaneous assembly synthesis and applications as pseudocapacitive materials, ChemSusChem, 8 (1) (2015), pp. 177-183

[44] K. Lu, D. Li, X. Gao, H. Dai, N. Wang, H. Ma, An advanced aqueous sodium-ion supercapacitor with a manganous hexacyanoferrate cathode and a Fe3O4/rGO anode, J. Mater. Chem. A, 3 (31) (2015), pp. 16013-16019

[45] Y. Wang, Y. Yang, X. Zhang, C. Liu, X. Hao, One-step electrodeposition of polyaniline/nickel hexacyanoferrate/sulfonated carbon nanotubes interconnected composite films for supercapacitor

J. Solid State Electrochem., 19 (10) (2015), pp. 3157-3168

[46] Z. Song, W. Liu, Q. Yuan, Q. Zhou, G. Liu, Z. Zhao, Microporous/mesoporous cobalt hexacyanoferrate nanocubes for long-cycle life asymmetric supercapacitors, J. Mater. Sci. Mater. Electron., 29 (17) (2018), pp. 14897-14905

[47] J.-.G. Wang, Z. Zhang, X. Zhang, X. Yin, X. Li, X. Liu, F. Kang, B. Wei, Cation exchange formation of prussian blue analogue submicroboxes for high-performance Na-ion hybrid supercapacitors, Nano Energy, 39 (2017), pp. 647-653

[48] X. Qiu, L. Li, Y. Sun, X. Kong, The application of nickel hexacyanoferrate/hexadecyl trimethyl ammonium bromide/graphene nanocomposites synthesized by reverse microemulsion in supercapacitors, Colloids Surf. A Physicochem. Eng. Asp., 506 (2016), pp. 670-677

[49] J. Chen, K. Huang, S. Liu, Insoluble metal hexacyanoferrates as supercapacitor electrodes

Electrochem. Commun., 10 (12) (2008), pp. 1851-1855